IEEE Access
Multidisciplinary | Rapid Review | Open Access Journal

Received February 5, 2018, accepted March 7, 2018, date of publication March 23, 2018, date of current version April 25, 2018.

Digital Object Identifier 10.1109/ACCESS.2018.2818938

Miniaturization of Broadband Stub Bandpass Filters Using Bridged-T Coils

CHIA-CHING HUANG, WEI-TING FANG, AND YO-SHEN LIN, (Senior Member, IEEE)
Department of Electrical Engineering, National Central University, Taoyuan 320, Taiwan

Corresponding author: Yo-Shen Lin (yslin@ee.ncu.edu.tw)

This work was supported in part by the Ministry of Science and Technology, Taiwan, under Grant MOST 103-2221-E-008-022 and Grant MOST 105-2628-E-008-001-MY3, in part by the National Chip Implementation Center, Taiwan, and in part by the National Center for High-Performance Computing, Taiwan.

ABSTRACT In this paper, broadband stub bandpass filters (BPFs) with very compact circuit sizes are proposed. Specifically, the circuit size of the conventional broadband stub BPF is largely reduced by replacing all transmission line sections with bridged-T coils. In addition, the design consideration regarding the use of cascaded bridged-T coils is investigated in detail. The proposed broadband BPF designs are based on lumped elements only, and they can be implemented using the integrated passive device process to achieve very compact circuit sizes. As an example, a miniature 7th-order broadband BPF with a passband from 4 to 12 GHz, which is to be used at the mixer's IF output of a radio astronomical receiver, is presented. The in-band insertion loss is within 2.46 ± 0.46 dB and the circuit size is only 2.30 mm $\times$ 2.03 mm. The long-lasting problem of large circuit size for conventional stub BPFs is thus solved.

INDEX TERMS Stub bandpass filter, bridged-T coil, integrated passive device, lumped element, miniaturization.

I. INTRODUCTION

Broadband bandpass filter (BPF) design at microwave frequencies is required in many practical applications. As an example, the Band-1 (35−50 GHz) receiver of Atacama Large Millimeter/submillimeter Array (ALMA) features a wide IF bandwidth from 4 to 12 GHz [1]. A broadband IF BPF with a passband from 4 to 12 GHz is thus required at the mixer's IF output. In addition, the design of ultra-wideband (UWB) BPF with a passband from 3.1 to 10.6 GHz still gathers much research attention in recent years, and various improved designs of UWB BPF with smaller circuit size and better stopband rejection have been proposed [2]–[9]. Conventionally, a broadband BPF design can be easily achieved by the stub BPF structures shown in Fig. 1(a) and 1(b) [10]. Especially, several highly-selective UWB BPFs [11]–[13] have been successfully achieved using the optimal distributed highpass filter structure shown in Fig. 1(b), which is essentially a wideband BPF. When designing it as a BPF, the optimal distributed highpass filter is composed of quarter-wavelength ($\lambda/4$) short stubs and half-wavelength ($\lambda/2$) unit elements between the shunt short stubs, and it is optimum in a sense that its unit elements and connecting lines are all non-redundant. As a result, a broadband BPF with high selectively can be achieved with a fewer number of stubs when compared with the stub BPF with $\lambda/4$ shunt stubs and $\lambda/4$ connecting lines in Fig. 1(a) [10].

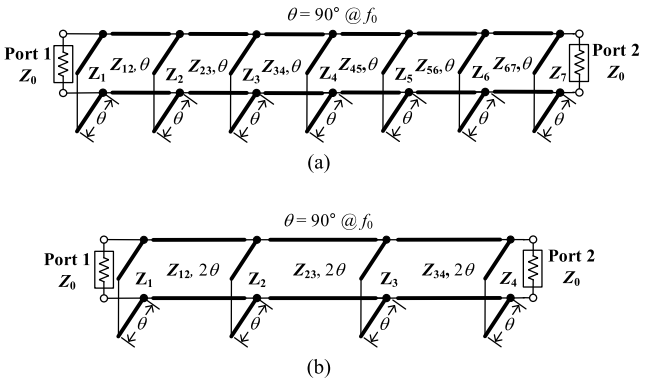

FIGURE 1. Circuit models of conventional stub bandpass filters. (a) The 7-th order stub bandpass filter with $\lambda/4$ shunt stubs and $\lambda/4$ connecting lines. (b) The optimal distributed highpass filter of 7th-order.

Due to the requirement of multiple transmission line sections of $\lambda/4$ or $\lambda/2$ long, the two stub BPF structures in Fig. 1 both exhibit a very large circuit size. For the design of ALMA Band-1 receiver front end, a compact IF BPF is

required because the receiver cartridge has limited space. In [14] and [15], bridged-T coils (BTCs) are used to realize wideband multi-mode resonator (MMR) BPFs with very compact sizes. The BTC [16], [17] can be regarded as a wideband lumped-element equivalent of a transmission line. As a result, when replacing all transmission line sections of the MMR with BTCs, the frequency response remains almost unchanged while the circuit size is largely reduced. Specifically, the UWB BPF in [15] features a very compact chip size of only 0.88 mm×0.88 mm. However, the compact MMR BPF designs in [14] and [15] are only third-order ones, and they cannot be easily extended to higher order filters for better selectivity because the synthesis method of higher order MMR BPF is not well established yet.

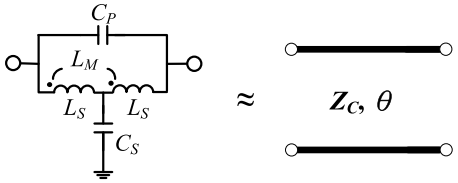

FIGURE 2. Circuit model of the bridged-T coil (BTC), which can be designed as a wideband lumped-element equivalent of a transmission line.

In this paper, to achieve a compact and highly selective IF BPF for the ALMA Band-1 receiver front end, the BTC in Fig. 2 is used to largely reduce the circuit sizes of conventional broadband stub BPFs. In addition, the design considerations regarding the use of cascaded BTCs is investigated in detail. The 7th-order stub BPF filter structure is chosen as the basis to achieve good frequency selectivity while a silicon-based integrated passive device (IPD) is used for chip implementation.

II. FILTER DESIGN

Shown in Fig. 1(a) is the conventional 7th-order stub BPF with λ/4 shunt stubs and λ/4 connecting lines. It can be easily designed for a given specification according to the design procedures in [10] and [18]. Considering a passband from 4 to 12 GHz and a reference impedance $Z_0 = 50\ \Omega$, the required line impedances for a 0.1-dB Chebyshev response can be obtained as: $Z_1 = Z_7 = 109.10\ \Omega$, $Z_2 = Z_6 = 111.74\ \Omega$, $Z_3 = Z_5 = 105.79\Omega$, $Z_4 = 103.68\ \Omega$, $Z_{12} = Z_{67} = 44.81\ \Omega$, $Z_{23} = Z_{56} = 48.74\ \Omega$, and $Z_{34} = Z_{45} = 51.26\ \Omega$. The filter's circuit simulated response is shown in Fig. 3(b), and a 7th-order bandpass response is obtained as expected.

According to Fig. 1(a), this 7th-order stub BPF exhibits a large circuit size of $3\lambda/2 \times \lambda/4$ at $f_0 = 8$ GHz. In order to largely reduce the circuit size, BTCs are utilized to replace all the λ/4 transmission line sections in Fig. 1(a). The resulted filter structure is illustrated in Fig. 3(a), in which each BTC has a circuit structure as shown in Fig. 2. Based on the line impedances and line lengths of the original stub BPF, the required L and C values of all BTCs in Fig. 3(a) can be solved by using the analytical design equations in [19], which

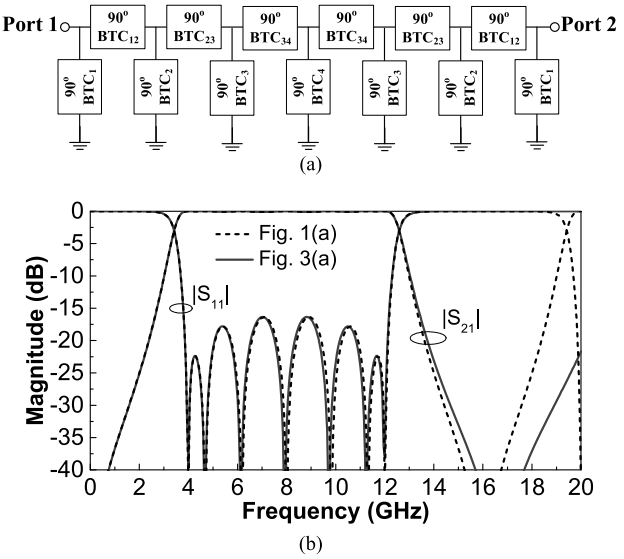

FIGURE 3. Proposed BTC-based stub bandpass filter realized by replacing each λ/4 line section in Fig. 1(a) with a BTC. (b) Comparison of circuit simulated frequency responses between the conventional stub bandpass filter in Fig. 1(a) and the BTC-based design.

are rearranged as the simpler form shown below:

$$C_S = \frac{2}{\frac{j\omega_a}{Y_{11a}+Y_{12a}} + \frac{\omega_a^2}{\omega_b^2-\omega_a^2}\left(\frac{j\omega_a}{Y_{11a}+Y_{12a}} - \frac{j\omega_b}{Y_{11b}+Y_{12b}}\right)} \quad (1)$$

$$C_P = \frac{1}{2(\omega_b^2-\omega_a^2)}\left(\frac{j\omega_a}{Z_{11a}-Z_{12a}} - \frac{j\omega_b}{Z_{11b}-Z_{12b}}\right) \quad (2)$$

$$L_S = \frac{1}{\frac{2j\omega_a}{Z_{11a}-Z_{12a}} + 4\omega_a^2 C_p} + \frac{1}{2(\omega_b^2-\omega_a^2)}\left(\frac{j\omega_a}{Y_{11a}+Y_{12a}} - \frac{j\omega_b}{Y_{11b}+Y_{12b}}\right) \quad (3)$$

$$L_M = \frac{1}{\frac{2j\omega_a}{Z_{11a}-Z_{12a}} + 4\omega_a^2 C_p} - \frac{1}{2(\omega_b^2-\omega_a^2)}\left(\frac{j\omega_a}{Y_{11a}+Y_{12a}} - \frac{j\omega_b}{Y_{11b}+Y_{12b}}\right) \quad (4)$$

where $\omega_a = 2\pi f_a$ and $\omega_b = 2\pi f_b$ while Z_{ija} and Z_{ijb} (or Y_{ija} and Y_{ijb}) are the Z-parameters (or Y-parameters) of the ideal transmission line at f_a and f_b. Given the required line impedance $Z_C = 1/Y_C$ and line length θ, the Z- and Y-parameters at f_a and f_b are first obtained by $Z_{11x} = Z_{22x} = -jZ_C/\tan\theta_x$, $Z_{12x} = Z_{21x} = -jZ_C/\sin\theta_x$, $Y_{11x} = Y_{22x} = -jY_C/\tan\theta_x$, and $Y_{12x} = Y_{21x} = jY_C/\sin\theta_x (x = a \text{ or } b)$, so (1) to (4) can be further modified as:

$$C_S = \frac{2}{\left(\frac{Z_C\omega_a\omega_b}{\omega_b^2-\omega_a^2}\right)\left(\frac{\omega_b\tan\theta_a\sin\theta_a}{\tan\theta_a-\sin\theta_a} - \frac{\omega_a\tan\theta_b\sin\theta_b}{\tan\theta_b-\sin\theta_b}\right)} \quad (5)$$

$$C_P = \frac{1}{2Z_C(\omega_b^2-\omega_a^2)}\left(\frac{\omega_a\tan\theta_a\sin\theta_a}{\tan\theta_a-\sin\theta_a} - \frac{\omega_b\tan\theta_b\sin\theta_b}{\tan\theta_b-\sin\theta_b}\right) \quad (6)$$

$$L_S = \frac{Z_C(\omega_b^2-\omega_a^2)}{2\omega_a\omega_b(\omega_b\cot\frac{\theta_a}{2} - \omega_a\cot\frac{\theta_b}{2})} \quad (7)$$

$$+\frac{Z_C}{2(\omega_b^2-\omega_a^2)}(\omega_a\cot\frac{\theta_a}{2}-\omega_b\cot\frac{\theta_b}{2})$$

$$L_M=\frac{Z_C(\omega_b^2-\omega_a^2)}{2\omega_a\omega_b(\omega_b\cot\frac{\theta_a}{2}-\omega_a\cot\frac{\theta_b}{2})}$$

$$-\frac{Z_C}{2(\omega_b^2-\omega_a^2)}(\omega_a\cot\frac{\theta_a}{2}-\omega_b\cot\frac{\theta_b}{2}) \quad (8)$$

Here, $f_a = 3.5$ GHz and $f_b = 12.5$ GHz are selected to solve for the L and C values so as to ensure the BTC-based equivalent transmission lines can support a bandwidth covering the required filter passband from 4 to 12 GHz. The L and C values of each BTC can then be calculated using (5) to (8) and the results are given in Table 1.

TABLE 1. Element values of bridged-T coils.

BTCs in Fig. 3(a)	$L_{S,x}$ (nH)	$L_{M,x}$ (nH)	$C_{S,x}$ (pF)	$C_{P,x}$ (pF)	Target line impedance, line length at f_0 = 8 GHz
$x = 1$	1.1685	0.5283	0.2851	0.02689	109.10 Ω, 90°
$x = 12$	0.4799	0.2170	0.6942	0.06548	44.81 Ω, 90°
$x = 2$	1.1968	0.5411	0.2784	0.02626	111.74 Ω, 90°
$x = 23$	0.5220	0.2360	0.6382	0.06020	48.74 Ω, 90°
$x = 3$	1.1330	0.5122	0.2940	0.02773	105.79 Ω, 90°
$x = 34$	0.5490	0.2482	0.6069	0.5724	51.26 Ω, 90°
$x = 4$	1.1104	0.5020	0.3000	0.02830	103.68 Ω, 90°

*f_a = 3.5 GHz and f_b = 12.5 GHz are used in solving the element values.

The circuit simulated frequency response of the resulted BTC-based stub BPF is compared with that of the conventional design in Fig. 3(b). The two frequency responses are identical at 3.5 and 12.5 GHz, and they are approximately the same around the filter's passband, indicating that the bandwidth of BTC is indeed large enough to cover the required passband. Notably, since the BTC-based stub BPF in Fig. 3(a) utilizes lumped elements only, its circuit size can be much smaller than the conventional stub BPF in Fig. 1(a).

Similarly, the BTC should be able to largely reduce the size of the conventional optimal distributed highpass filter as shown in Fig. 1(b). The optimal distributed highpass filter in Fig. 1(b) is composed of four λ/4 shunt stubs ($n = 4$) and three λ/2 connecting lines, which is capable of achieving a 7th-order bandpass response. Its design procedure for a given specification has been well established [10]. Here, in order to achieve a passband from 4 to 12 GHz, the center frequency f_0 is set as 8 GHz and $\theta_C = 45°$ (or $\pi/4$) is chosen. The resulted passband will be from $f_0 \times \theta_C/(\pi/2) = 4$ GHz to $f_0 \times (\pi - \theta_C)/(\pi/2) = 12$ GHz. This optimal distributed highpass filter is designed with a 0.1-dB equal-ripple passband and the normalized line admittances required can be obtained by extrapolating the values for $n = 4$ in [10, Table 6.1] as: $y_1 = y_4 = 0.76943$, $y_{1,2} = y_{3,4} = 0.92334$, $y_2 = y_3 = 1.18814$, and $y_{2,3} = 0.88395$. For a reference impedance $Z_0 = 50$ Ω, all the required line impedances in Fig. 1(b) can then be obtained as: $Z_1 = Z_4 = 64.98$ Ω, $Z_{1,2} = Z_{3,4} = 54.15$ Ω, $Z_2 = Z_3 = 42.08$ Ω, and $Z_{2,3} = 56.56$ Ω. The corresponding circuit simulated response is shown in Fig. 4(b), and the desired 7th-order bandpass response is observed.

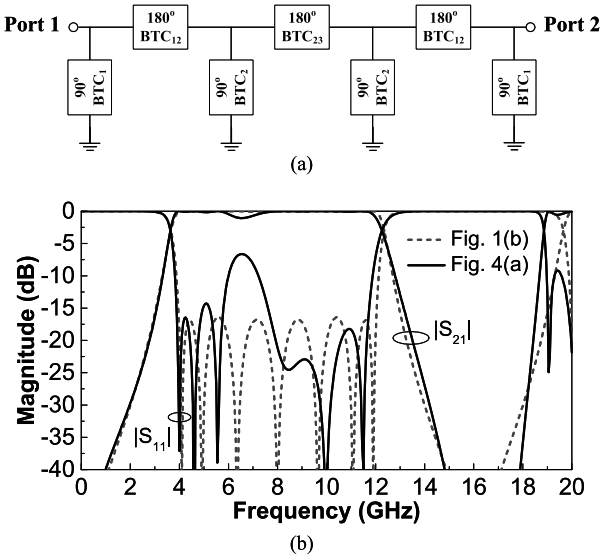

FIGURE 4. (a) Proposed BTC-based optimal distributed highpass filter realized by replacing each λ/4 or λ/2 line section in Fig. 1(b) with a BTC. (b) Comparison of circuit simulated frequency responses between the conventional optimal distributed highpass filter in Fig. 1(b) and the BTC-based design.

TABLE 2. Element values of bridged-T coils.

BTCs in Fig. 4(a)	$L_{S,x}$ (nH)	$L_{M,x}$ (nH)	$C_{S,x}$ (pF)	$C_{P,x}$ (pF)	Target line impedance, line length at f_0 = 8 GHz
$x = 1$	0.6959	0.3146	0.4787	0.04515	64.98 Ω, 90°
$x = 12$	1.3109	0.1441	0.9924	0.1990	54.15 Ω, 180°
$x = 2$	0.4507	0.2038	0.7392	0.06972	42.08 Ω, 90°
$x = 23$	1.3692	0.1505	0.9501	0.1905	56.56 Ω, 180°

*f_a = 3.5 GHz and f_b = 12.5 GHz are used in solving the element values.

Again, this 7th-order BPF exhibits a large circuit size of 3λ/2×λ/4 at $f_0 = 8$ GHz, and we should be able to reduce the circuit size by replacing all its λ/4 and λ/2 transmission line sections with BTCs. The resulted circuit model is shown in Fig. 4(a). The required L and C values for each BTC can be obtained using (5)-(8) and the results are given in Table 2. Here, $f_a = 3.5$ GHz and $f_b = 12.5$ GHz is again chosen in solving the element values so as to achieve a good match with the original transmission-line based BPF across the passband. As shown in Fig. 4(b), although the BTC-based BPF features exactly the same S_{11} and S_{21} as the optimal distributed highpass filter at 3.5 and 12.5 GHz, it does not exhibit a good in-band response and the input matching is rather poor. This is much different from the case in Fig. 3(b) in which the BTC-based stub BPF features almost the same frequency response as its transmission-line based counterpart.

The poor performance of the BTC-based BPF as observed in Fig. 4(b) is due to the limited bandwidth of BTC. According to [20], the BTC exhibits a bandwidth up to an electrical length of π. As a result, the 180° BTC in Fig. 4(a) cannot support the required bandwidth for its equivalent electrical length at 12.5 GHz is already 281.25°. This can be

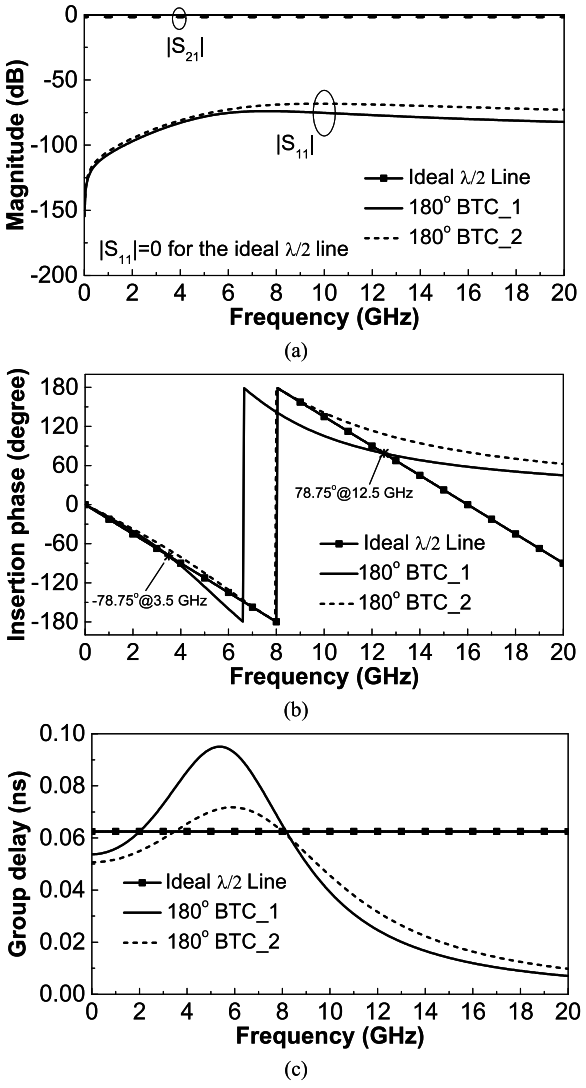

FIGURE 5. Comparison of circuit simulated frequency responses of the ideal λ/2 transmission line with a characteristic impedance $Z_{12} = 54.15\ \Omega$ and the corresponding BTCs with an equivalent electrical length of 180° at $f_0 = 8$ GHz. For 180° BTC_1, $f_a = 3.5$ GHz and $f_b = 12.5$ GHz are used for solving the L and C values. For 180° BTC_2, $f_a = 7.8$ GHz and $f_b = 8.2$ GHz are used instead. (a) Insertion loss and return loss. (b) Insertion phase. (c) Group delay. Reference impedances of all S-parameters are equal to 54.15 Ω.

examined in detail by comparing the frequency responses of the ideal λ/2 transmission line and the corresponding 180° BTC in Fig. 5. Here, the transmission line section Z_{12} in Fig. 1(b) with a characteristic impedance of 54.15 Ω and an electrical length of 180° at $f_0 = 8$ GHz is used as an example. The L and C of the corresponding BTC, i.e., 180° BTC_1 are those listed in the second row of Table 2, which are solved with $f_a = 3.5$ GHz and $f_b = 12.5$ GHz. According to Fig. 5(a), this 180° BTC_1 is well matched to 54.15 Ω with a return loss better than 68.2 dB from dc up to 20 GHz. In addition, its insertion phase is exactly equal to the desired values of $-180° \times f_a/f_0 = -78.75°$ at $f_a = 3.5$ GHz and $-180° \times f_b/f_0 = -281.25°$ or 78.75° at $f_b = 12.5$ GHz according to Fig. 5(b). However, its insertion phase responses deviates a lot from that of the ideal λ/2 line between these two frequencies, such that its equivalent electrical length becomes far from the desired value of 180° at $f_0 = 8$ GHz. In addition, it does not exhibit good linearity as can be told from the group delay response given in Fig. 5(c). These give rise to the poor in-band response of the BTC-based BPF design as observed in Fig. 4(b).

Alternatively, if the two frequencies used to solve for the L and C values (i.e., f_a and f_b) are closer to f_0, the accuracy in equivalent electrical length of the 180° BTC around f_0 can be much improved. By setting $f_a = 7.8$ GHz and $f_b = 8.2$ GHz instead, a new 180° BTC, i.e., 180° BTC_2 is obtained. The corresponding element values are: $L_{S,12} = 1.1092$ nH, $L_{M,12} = 0.2626$ nH, $C_{S,12} = 0.9357$ pF, $C_{P,12} = 0.1443$ pF. According to Fig. 5(a) and 5(b), this new 180° BTC is also well matched to 54.15 Ω up to 20 GHz, while its insertion phase is exactly equal to 180° at $f_0 = 8$ GHz. However, its insertion phases at 3.5 and 12.5 GHz now deviate a lot from the desired values of −78.75° and 78.75°, respectively. Also, it does not feature good linearity as well according to the group delay response given in Fig. 5(c). As a result, if $f_a = 7.8$ GHz and $f_b = 8.2$ GHz are used instead for all the three 180° BTCs in Fig. 4(a), the resulted BTC-based optimal distributed highpass filter still does not exhibit the desired frequency response. As shown in Fig. 6, although a better in-band response is obtained with these new 180° BTCs, the bandwidth of the resulted BPF becomes much larger than the original transmission line-based design in Fig. 1(b).

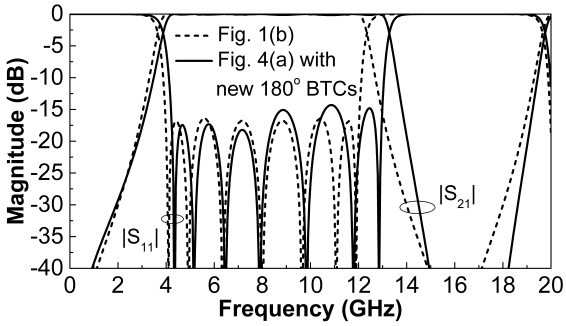

FIGURE 6. Comparison of circuit simulated frequency responses between the conventional optimal distributed highpass filter in Fig. 1(b) and the BTC-based design in Fig. 4(a). For the BTC-based design, $f_a = 7.8$ GHz and $f_b = 8.2$ GHz are used in solving the element values of the 180° BTCs. The results are: $L_{S,12} = 1.1092$ nH, $L_{M,12} = 0.2626$ nH, $C_{S,12} = 0.9357$ pF, $C_{P,12} = 0.1443$ pF, $L_{S,23} = 1.1585$ nH, $L_{M,23} = 0.2743$ nH, $C_{S,23} = 0.8958$ pF, and $C_{P,23} = 0.1382$ pF.

The abovementioned problem with the size reduction of an optimal distributed highpass filter using BTCs can be tackled by employing the cascade of multiple BTCs. As shown in Fig. 7(a), if each λ/2 unit element between the shunt stubs in Fig. 1(b) is realized with the cascade of two 90° BTCs, the bandwidth of the resulted BTC-based equivalent transmission line can be extended to $2f_0 = 16$ GHz, which is enough to cover the passband of this optimal distributed

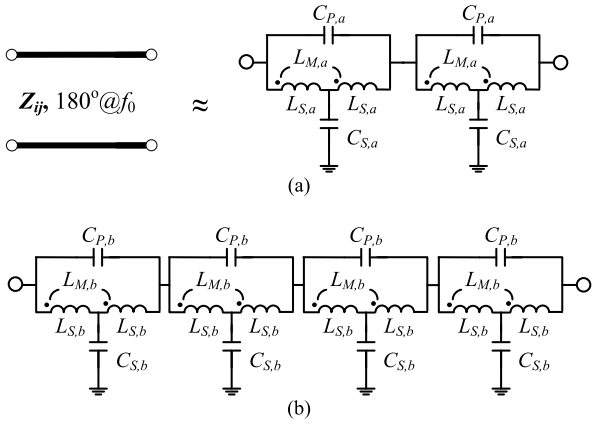

FIGURE 7. Replacing the λ/2 transmission line section in an optimal distributed highpass filter with multiple BTCs in cascade. (a) Two BTCs of 90° equivalent electrical length in cascade. (b) Four BTCs of 45° equivalent electrical length in cascade.

TABLE 3. Element values of bridged-T coils.

BTCs in Fig. 9(a)	$L_{S,x}$ (nH)	$L_{M,x}$ (nH)	$C_{S,x}$ (pF)	$C_{P,x}$ (pF)	Target line impedance, line length at f_0 = 8.2 GHz
x = 1	0.6959	0.3146	0.4787	0.04515	64.98 Ω, 90°
x = 12	0.5800	0.2622	0.5744	0.05418	54.15 Ω, 90°
x = 2	0.4507	0.2038	0.7392	0.06972	42.08 Ω, 90°
x = 23	0.6058	0.2739	0.5499	0.05187	56.56 Ω, 90°

*f_a = 3.5 GHz and f_b = 12.5 GHz are used in solving the element values.

highpass filter design. Also, if the cascade of four 45° BTCs is employed instead as shown in Fig. 7(b), the bandwidth can be further extended to $4f_0$. This can be verified by comparing the frequency responses of the ideal λ/2 line and the cascade of BTCs as shown in Fig. 8, in which the ideal λ/2 line of characteristic impedance $Z_{12} = 54.15\ \Omega$ is again used as an example. In order to achieve a good match to the ideal λ/2 line within the filter's passband, $f_a = 3.5$ GHz and $f_b = 12.5$ GHz are used to solve for the L and C values of these BTCs. For the 90° BTC with an equivalent characteristic impedance of 54.15 Ω, its element values are given in the second row of Table 3. For the 45° BTC with an equivalent characteristic impedance of 54.15 Ω, its element values are those in the second row of Table 4. According to Fig. 8(a), both the cascade of two 90° BTCs and the cascade of four 45° BTCs are well matched to 54.15 Ω as desired. Notably, both of them exhibit an insertion phase response almost identical to that of the ideal λ/2 line between 3.5 and 12.5 GHz. In addition, both of them feature a much more linear frequency response compared to those 180° BTCs in Fig. 5 according to Fig. 8(c). Especially, the cascade of four 45° BTCs features the largest bandwidth as expected. Its frequency response is in very good agreement with the ideal λ/2 line up to 20 GHz.

Therefore, the poor performance of the BTC-based optimal distributed highpass filter in Fig. 4(a) can be much improved by employing the cascade of BTCs of a smaller equivalent

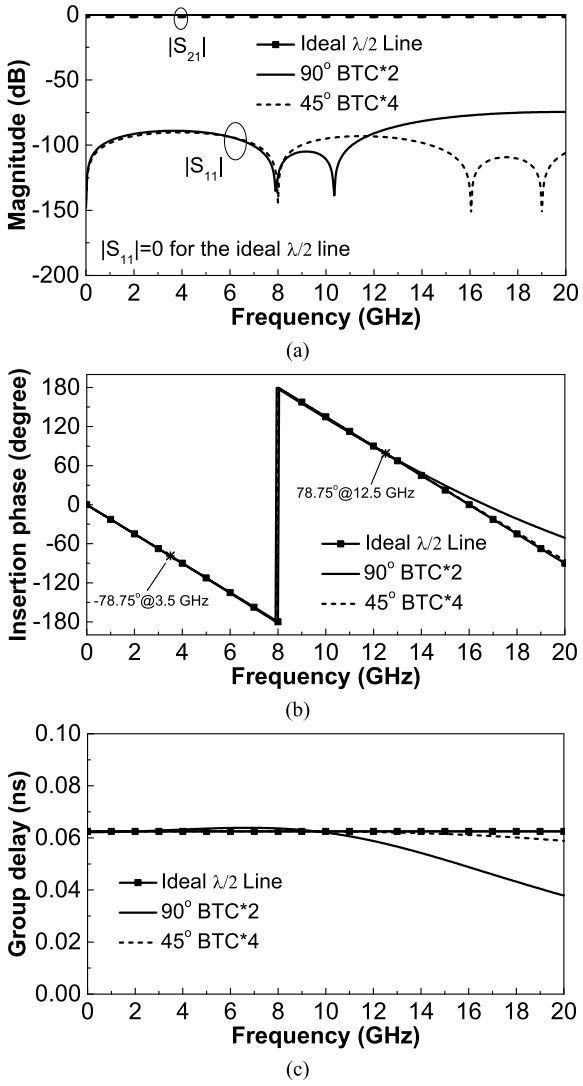

FIGURE 8. Comparison of circuit simulated frequency responses of the ideal λ/2 transmission line with a characteristic impedance $Z_{12} = 54.15\ \Omega$, the cascade of two 90° BTCs, and the cascade of four 45° BTCs. The frequencies used in solving the L and C values are $f_a = 3.5$ GHz and $f_b = 12.5$ GHz. (a) Insertion loss and return loss. (b) Insertion phase. (c) Group delay. Reference impedances of all S-parameters are equal to 54.15 Ω.

electrical length as shown in Fig. 9. Specifically, the BTC-based optimal distributed highpass filter in Fig. 9(a) uses two 90° BTCs in cascade to replace each λ/2 unit element and one 90° BTC to replace each λ/4 shunt stub. On the other hand, the BTC-based optimal distributed highpass filter in Fig. 9(b) uses four 45° BTCs in cascade to replace a λ/2 unit element and two 45° BTCs to replace each λ/4 shunt stub. The corresponding element values are given in Table 3 and 4, and the circuit simulated frequency responses are given in Fig. 10. Both of the two BTC-based optimal distributed highpass filters feature almost identical in-band frequency responses as the conventional design in Fig. 1(b), while the response of the 45° BTC-based design is well matched to the conventional design up to 20 GHz.

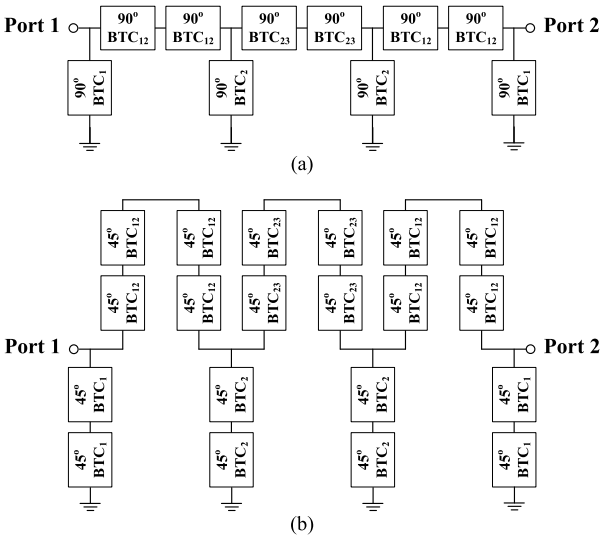

FIGURE 9. Proposed BTC-based optimal distributed highpass filter designs using cascaded BTCs of different equivalent electrical lengths. (a) 90° BTC-based filter design. (b) 45° BTC-based filter design.

TABLE 4. Element values of bridged-T coils.

BTCs in Fig. 9(b)	$L_{S,x}$ (nH)	$L_{M,x}$ (nH)	$C_{S,x}$ (pF)	$C_{P,x}$ (pF)	Target line impedance, line length at f_0 = 8.2 GHz
x = 1	0.3407	0.1668	0.2404	0.02060	64.98 Ω, 45°
x = 12	0.2840	0.1390	0.2885	0.02472	54.15 Ω, 45°
x = 2	0.2207	0.1080	0.3712	0.03181	42.08 Ω, 45°
x = 23	0.2966	0.1452	0.2762	0.02367	56.56 Ω, 45°

*f_a = 3.5 GHz and f_b = 12.5 GHz are used in solving the element values.

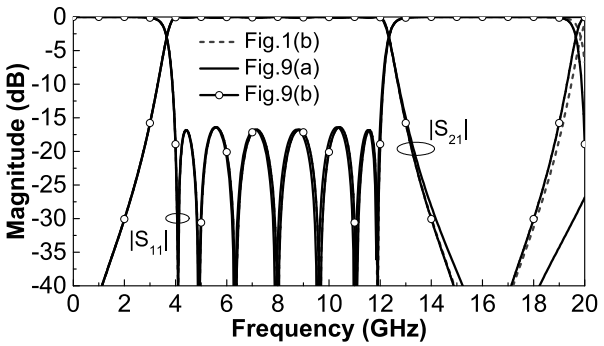

FIGURE 10. Circuit simulated results of the two BTC-based optimal distributed highpass filter designs in Fig. 9 and the conventional design in Fig. 1(b). f_a = 3.5 GHz and f_b = 12.5 GHz are used in solving the element values of BTC.

Notably, although the 45° BTC-based design in Fig. 9(b) requires twice as more BTCs as compared to the 90° BTC-based design in Fig. 9(a), the L and C values of each 45° BTC are smaller so the total filter size will not increase. The size reduction of conventional optimal distributed highpass filter can thus be successfully achieved with these BTC-based designs.

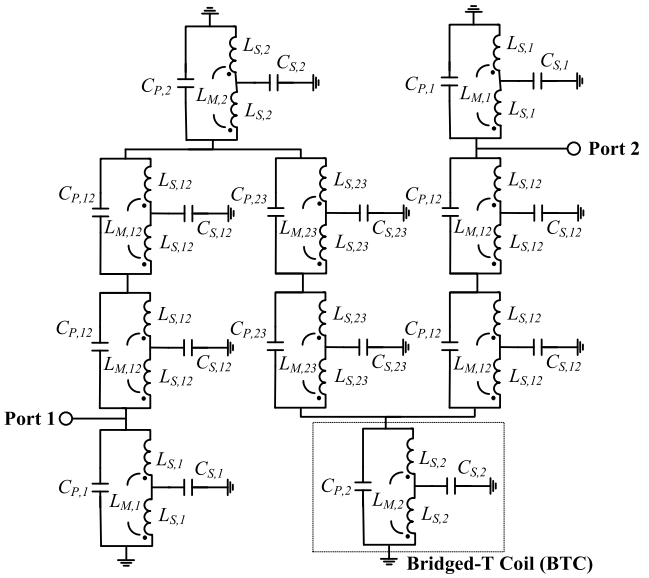

FIGURE 11. Circuit model of proposed BTC-based stub bandpass filter.

III. FILTER IMPLEMENTATION

Comparing the BTC-based filter designs in Fig. 3 and Fig. 9, the two designs in Fig. 9 requires a fewer number of stubs so they may exhibit lower insertion loss in practice. In addition, although the insertion loss response of the 90° BTC-based filter design in Fig. 9(a) is not as close to the conventional optimal distributed highpass filter as the 45° BTC-based design in Fig. 9(b), it features better stopband rejection at 20 GHz. Therefore, the 90° BTC-based optimal distributed highpass filter as shown in Fig. 11 is selected to implement the proposed 4-12 GHz BPF for ALMA Band-1 receiver.

Here, in order to achieve a passband from 4 to 12 GHz, the center frequency f_0 is set as 8.2 GHz and $\theta_C = 40°$ (or 0.22π) is chosen. The resulted passband will be from $f_0 \times \theta_C/(\pi/2) = 3.64$ GHz to $f_0 \times (\pi - \theta_C)/(\pi/2) = 12.75$ GHz. The slightly wider passband of the lossless filter design is to ensure that the fabricated filter would properly cover the required passband of 4 to 12 GHz. Also, the slighter higher f_0 can help reduce the passband insertion loss around the BPF's upper cutoff frequency. The proposed filter is designed with a 0.1-dB equal-ripple passband and the normalized line admittances required can be obtained by extrapolating the values for $n = 4$ in [10, Table 6.1] as: $y_1 = y_4 = 0.59551$, $y_{1,2} = y_{3,4} = 0.98453$, $y_2 = y_3 = 0.86984$, and $y_{2,3} = 0.95505$. For a reference impedance $Z_0 = 50\ \Omega$, all the required line impedances in Fig. 1(b) can be obtained as: $Z_1 = Z_4 = 83.96\ \Omega$, $Z_{1,2} = Z_{3,4} = 50.78\ \Omega$, $Z_2 = Z_3 = 57.48\ \Omega$, and $Z_{2,3} = 52.35\ \Omega$.

Based on the above line impedances, the required L and C values of each 90° BTCs in Fig. 11 can then be calculated using (5) to (8). In order to examine how the selection of f_a and f_b affects the filter's frequency response, four sets of (f_a, f_b) are used in solving the element values of BTC and the

TABLE 5. Element values of bridged-T coils.

BTCs in Fig. 11	$L_{S,x}$ (nH)	$L_{M,x}$ (nH)	$C_{S,x}$ (pF)	$C_{P,x}$ (pF)	Target line impedance, line length at f_0 = 8.2 GHz
$x = 1$	0.8665	0.4013	0.3597	0.03299	83.96 Ω, 90°
$x = 12$	0.5240	0.2427	0.5947	0.05455	50.78 Ω, 90°
$x = 2$	0.5931	0.2748	0.5254	0.04819	57.48 Ω, 90°
$x = 23$	0.5402	0.2502	0.5769	0.05291	52.35 Ω, 90°

*f_a = 8 GHz and f_b = 8.4 GHz are used in solving the element values.

TABLE 6. Element values of bridged-T coils.

BTCs in Fig. 11	$L_{S,x}$ (nH)	$L_{M,x}$ (nH)	$C_{S,x}$ (pF)	$C_{P,x}$ (pF)	Target line impedance, line length at f_0 = 8.2 GHz
$x = 1$	0.8680	0.4022	0.3604	0.03304	83.96 Ω, 90°
$x = 12$	0.5250	0.2432	0.5958	0.05463	50.78 Ω, 90°
$x = 2$	0.5943	0.2753	0.5264	0.04827	57.48 Ω, 90°
$x = 23$	0.5412	0.2508	0.5780	0.05300	52.35 Ω, 90°

*f_a = 6 GHz and f_b = 10 GHz are used in solving the element values.

TABLE 7. Element values of bridged-T coils.

BTCs in Fig.11	$L_{S,x}$ (nH)	$L_{M,x}$ (nH)	$C_{S,x}$ (pF)	$C_{P,x}$ (pF)	Target line impedance, line length at f_0 = 8.2 GHz
$x = 1$	0.8761	0.3984	0.3616	0.03388	83.96 Ω, 90°
$x = 12$	0.5299	0.2410	0.5979	0.05602	50.78 Ω, 90°
$x = 2$	0.5998	0.2728	0.5282	0.04949	57.48 Ω, 90°
$x = 23$	0.5462	0.2484	0.5800	0.05434	52.35 Ω, 90°

*f_a = 3.5 GHz and f_b = 12.5 GHz are used in solving the element values.

TABLE 8. Element values of bridged-T coils.

BTCs in Fig.11	$L_{S,x}$ (nH)	$L_{M,x}$ (nH)	$C_{S,x}$ (pF)	$C_{P,x}$ (pF)	Target line impedance, line length at f_0 = 8.2 GHz
$x = 1$	0.8897	0.3895	0.3629	0.03548	83.96 Ω, 90°
$x = 12$	0.5381	0.2356	0.6001	0.05866	50.78 Ω, 90°
$x = 2$	0.6091	0.2667	0.5301	0.05182	57.48 Ω, 90°
$x = 23$	0.5547	0.2429	0.5821	0.05690	52.35 Ω, 90°

*f_a = 1 GHz and f_b = 15 GHz are used in solving the element values.

results are given in Table 5 to 8. The corresponding circuit simulated filter frequency responses are shown in Fig. 12. For the case with $(f_a, f_b) = (8\text{ GHz}, 8.4\text{ GHz})$ in Fig. 12(a), a very good match to the conventional optimal distributed highpass filter around $f_0 = 8.2$ GHz is obtained. However, the accuracy in passband bandwidth is not very good. As f_a and f_b move closer to the passband edges, a better agreement in passband bandwidth can be obtained with a slight discrepancy on the in-band return loss response and the out-of-band insertion loss response. With $(f_a, f_b) = (1\text{ GHz}, 15\text{ GHz})$ in Fig. 12(d), a better matching of the out-of-band rejection is obtained at the expense of larger error in passband bandwidth. Therefore, the design with $(f_a, f_b) = (3.5\text{ GHz}, 12.5\text{ GHz})$ in Fig. 12(c) is selected for circuit implementation.

The proposed filter is implemented using the silicon-based IPD process provided by the Advanced Furnace Systems

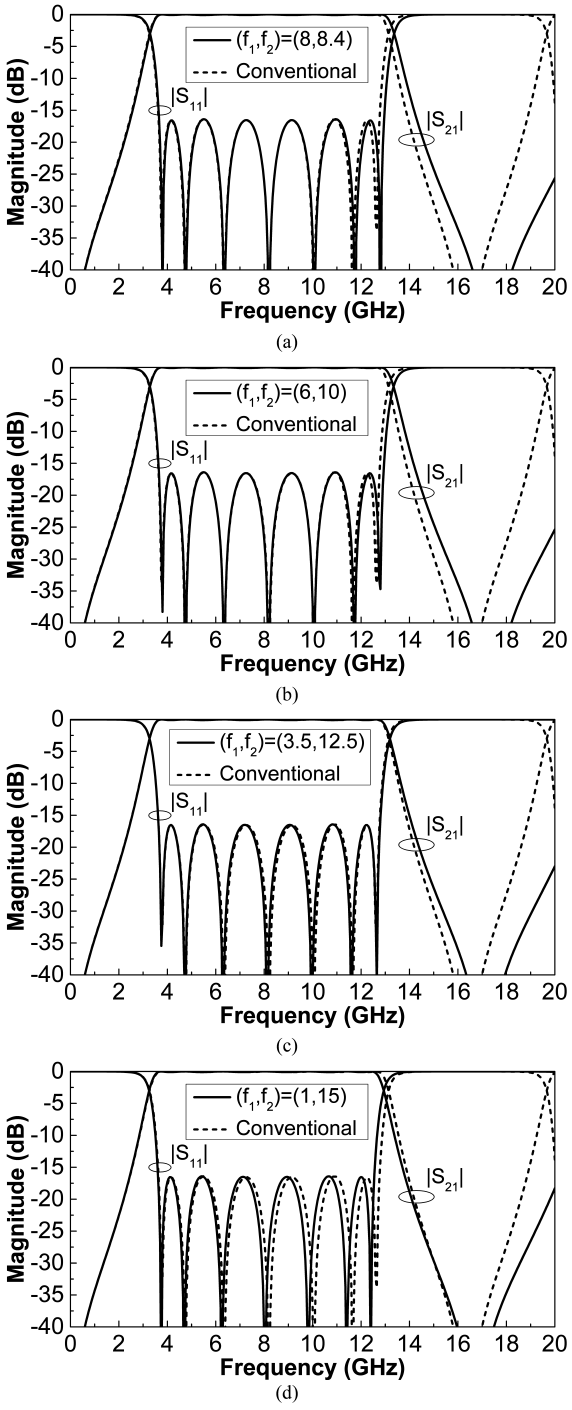

FIGURE 12. Comparison of circuit simulated results of the proposed BTC-based stub bandpass filter design in Fig. 11 and the conventional design in Fig. 1(b) for different selections of (f_a, f_b) in solving the element values. (a) f_a = 8 GHz and f_b = 8.4 GHz. (b) f_a = 6 GHz and f_b = 10 GHz. (c) f_a = 3.5 GHz and f_b = 12.5 GHz. (d) f_a = 1 GHz and f_b = 15 GHz.

Corp., and its simplified layer structure is shown in Fig. 13(a). Each BTC in Fig. 11 is realized in IPD by the combination of a center-tapped balanced spiral inductor and metal-insulator-metal (MIM) capacitors according to the layout

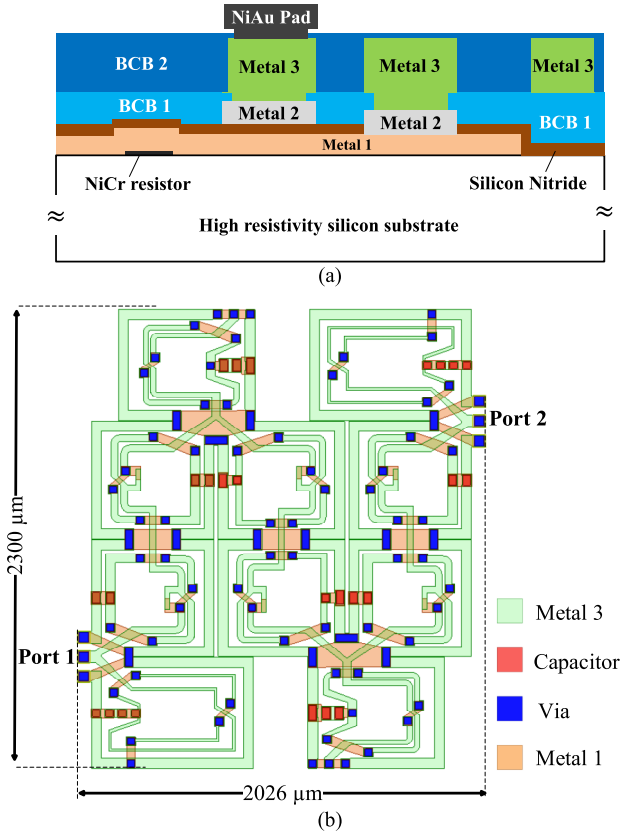

FIGURE 13. (a) Simplified layer structure of the silicon-based integrated passive device (IPD) process used for filter implementation. (b) IPD Layout of proposed miniaturized broadband BTC-based stub bandpass filter in Fig. 11.

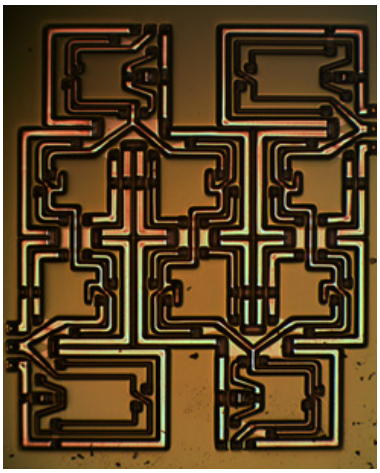

FIGURE 14. Photograph of the proposed miniaturized broadband BTC-based stub bandpass filter in IPD. Circuit size: 2.30 mm × 2.03 mm.

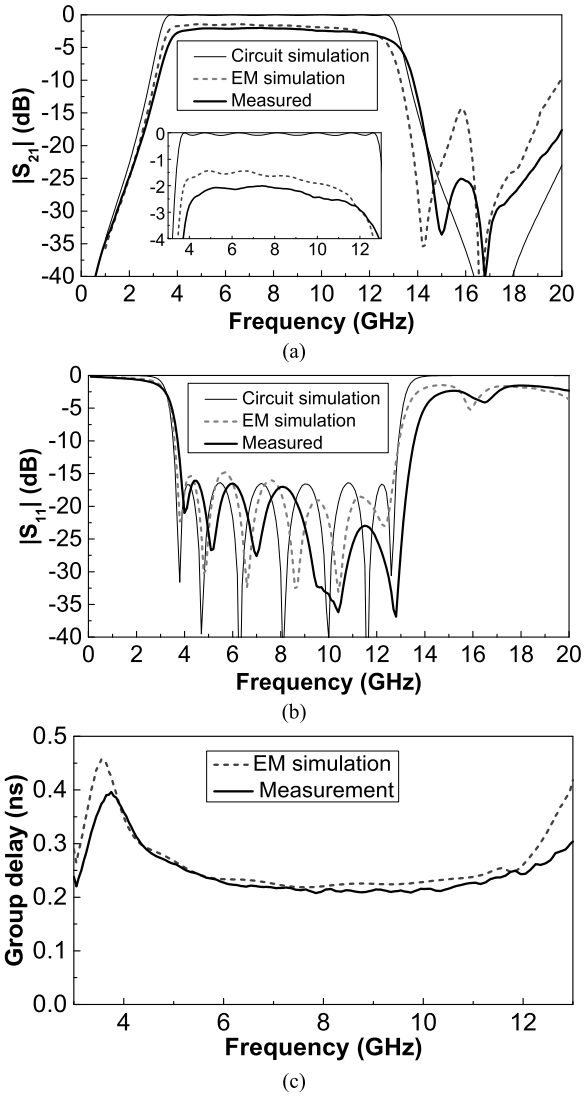

FIGURE 15. Measured and EM simulated frequency responses of proposed miniaturized broadband BTC-based stub bandpass filter in IPD. (a) Insertion loss. (b) Return loss. (c) In-band group delay.

method detailed in [14], [15], and [19]. To determine the geometrical parameters, the full-wave simulated Z- and Y-parameters of each BTC in IPD are input into (1) and (4) to extract the equivalent L and C values. The geometrical parameters of the spiral inductors and MIM capacitors are then adjusted accordingly until the extracted L and C values match with the design targets in Table 7 with minimum errors. After the layout designs of all BTCs are completed, they are connected based on the filter circuit model in Fig. 11. Also, the layout is properly arranged to achieve a compact filter size as shown in Fig. 13(b).

The photograph of the fabricated filter is shown in Fig. 14, and it is measured using the on-wafer-probing technique with ground-signal-ground (GSG) probes. The measured and EM simulated results are shown in Fig. 15. The measured in-band insertion loss is better than 2.92 dB from 4 to 12 GHz with a minimum insertion loss of 2 dB at 7.4 GHz. The slightly larger insertion loss is mainly due to the higher conductor loss caused by the thin conductor traces used for realizing the BTCs. The measured in-band return loss is greater than 16.1 dB. The measured frequency response shifts to a higher frequency as compared with the EM simulated one, which is

attributed to the process variation of the MIM capacitors. The in-band group delay in Fig. 15(c) is within 0.283±0.075 ns.

TABLE 9. Performance comparison with other recent works on compact broadband bandpass filter design.

	[2]	[14]	[15]	This work
Technology	Silicon-Based IPD	Glass-Based IPD	GaAs pHEMT	Silicon-Based IPD
Topology	Highpass & Lowpass Filters	Bridged-T Coil-Based MMR BPF	Bridged-T Coil-Based MMR BPF	Bridged-T Coil-Based Stub BPF
Filter order	3rd-order	3rd-order	3rd-order	7th-order
Bandwidth (GHz)	3–10.6	3.1–10.6	3.1–10.6	4–12
Circuit size (mm × mm)	2.9 × 2.4	2.21 × 1.04	0.88 × 0.88	2.30 × 2.03
Electrical size	$0.066\lambda_0 \times 0.055\lambda_0$ at 6.85 GHz	$0.050\lambda_0 \times 0.024\lambda_0$ at 6.85 GHz	$0.020\lambda_0 \times 0.020\lambda_0$ at 6.85 GHz	$0.061\lambda_0 \times 0.054\lambda_0$ at 8 GHz
In-band insertion loss	< 2.3 dB*	< 1.47 dB	< 2.37 dB	< 2.92 dB

*Estimated from graph

Table 9 compares the measured performance of proposed filter with other recent works on miniaturized broadband BPF design of similar fractional bandwidth. The proposed design is smaller than the lumped UWB BPF that is also realized in a silicon-based IPD process [2]. Comparing to the BTC-based MMR BPFs in [14] and [15], the proposed design is larger in size but it features much better frequency selectivity for the filter designs in [14] and [15] are only 3rd-order ones.

IV. CONCLUSION

In this work, by using BTCs to replace transmission lines and by adopting the IPD process for circuit implementation, a broadband stub BPF with very compact circuit size and good frequency selectivity is achieved. Better frequency selectivity can also be easily achieved by extending the proposed design to higher order ones at the expense of larger circuit size and higher loss. The long-lasting problem of large circuit size for conventional stub BPFs can thus be removed by using the proposed design method.

REFERENCES

[1] S.-H. Weng *et al.*, "A 35–50 GHz triple cascode mixer module with intermediate frequency of 4–12 GHz based on low noise GaAs PHEMT process," in *Proc. IEEE Int. Symp. Radio-Freq. Integr. Technol. (RFIT)*, Aug. 2016, pp. 1–3.
[2] Z. Wu, Y. Shim, and M. Rais-Zadeh, "Miniaturized UWB filters integrated with tunable notch filters using a silicon-based integrated passive device technology," *IEEE Trans. Microw. Theory Techn.*, vol. 60, no. 3, pp. 518–527, Mar. 2012.
[3] Z. Shang *et al.*, "Design of a superconducting ultra-wideband (UWB) bandpass filter with sharp rejection skirts and miniaturized size," *IEEE Microw. Wireless Compon. Lett.*, vol. 23, no. 2, pp. 72–74, Feb. 2013.
[4] K. U. Ahmed and B. S. Virdee, "Ultra-wideband bandpass filter based on composite right/left handed transmission-line unit-cell," *IEEE Trans. Microw. Theory Techn.*, vol. 61, no. 2, pp. 782–788, Feb. 2013.
[5] X. Li and X. Ji, "Novel compact UWB bandpass filters design with cross-coupling between λ/4 short-circuited stub," *IEEE Microw. Wireless Compon. Lett.*, vol. 24, no. 1, pp. 23–25, Jan. 2014.
[6] X. Lu *et al.*, "Superconducting ultra-wideband (UWB) bandpass filter design based on quintuple/quadruple/ triple-mode resonator," *IEEE Trans. Microw. Theory Techn.*, vol. 63, no. 4, pp. 1281–1293, Apr. 2015.
[7] A. Taibi, M. Trabelsi, A. Slimane, M. T. Belaroussi, and J. P. Raskin, "A novel design method for compact UWB bandpass filters," *IEEE Microw. Wireless Compon. Lett.*, vol. 25, no. 1, pp. 4–6, Jan. 2015.
[8] S.-W. Lan, M.-H. Weng, C.-Y. Hung, and S.-J. Chang, "Design of a compact ultra-wideband bandpass filter with an extremely broad stopband region," *IEEE Microw. Wireless Compon. Lett.*, vol. 26, no. 6, pp. 392–394, Jun. 2016.
[9] C.-X. Zhou, P.-P. Guo, K. Zhou, and W. Wu, "Design of a compact UWB filter with high selectivity and superwide stopband," *IEEE Microw. Wireless Compon. Lett.*, vol. 27, no. 7, pp. 636–638, Jul. 2017.
[10] J.-S. Hong, *Microstrip Filters for RF/Microwave Applications*, 2nd ed. Hoboken, NJ, USA: Wiley, 2011, ch. 6.
[11] J.-S. Hong and H. Shaman, "An optimum ultra-wideband microstrip filter," *Microw. Opt. Technol. Lett.*, vol. 47, no. 3, pp. 230–233, 2005.
[12] W.-T. Wong, Y.-S. Lin, C.-H. Wang, and C. H. Chen, "Highly selective microstrip bandpass filters for ultra-wideband (UWB) applications," in *Proc. Asia–Pacific Microw. Conf.*, Nov. 2005, p. 4.
[13] H. Shaman and J.-S. Hong, "A novel ultra-wideband (UWB) bandpass filter (BPF) with pairs of transmission zeroes," *IEEE Microw. Wireless Compon. Lett.*, vol. 17, no. 2, pp. 121–123, Feb. 2007.
[14] W.-T. Fang, T.-H. Tseng, and Y.-S. Lin, "Miniaturized ultra-wideband bandpass filter using bridged-T coil," *IEEE Microw. Wireless Compon. Lett.*, vol. 24, no. 6, pp. 367–369, Jun. 2014.
[15] T.-H. Tseng, W.-T. Fang, and Y.-S. Lin, "Super compact and ultra-wideband bandpass filter using bridged-T coils," in *IEEE MTT-S Int. Microw. Symp. Dig.*, May 2016, pp. 1–3.
[16] E. L. Ginzton, W. R. Hewlett, J. H. Jasberg, and J. D. Noe, "Distributed amplification," *Proc. IRE*, vol. 36, no. 8, pp. 956–969, Aug. 1948.
[17] E. M. Chase and W. Kennan, "A power distributed amplifier using constant-R networks," in *IEEE MTT-S Int. Microw. Symp. Dig.*, Jun. 1986, pp. 811–815.
[18] G. L. Matthaei, E. M. T. Jones, and L. Young, *Microwave Filters, Impedance-Matching Networks, and Coupling Structures*. New York, NY, USA: McGraw-Hill, 1964, ch. 10.
[19] Y.-S. Lin and J.-H. Lee, "Miniature Butler matrix design using glass-based thin-film integrated passive device technology for 2.5-GHz applications," *IEEE Trans. Microw. Theory Techn.*, vol. 61, no. 7, pp. 2594–2602, Jul. 2013.
[20] T.-S. Horng, J.-M. Wu, L.-Q. Yang, and S.-T. Fang, "A novel modified-T equivalent circuit for modeling LTCC embedded inductors with a large bandwidth," *IEEE Trans. Microw. Theory Techn.*, vol. 51, no. 12, pp. 2327–2333, Dec. 2003.

CHIA-CHING HUANG was born in Changhua, Taiwan, in 1990. She received the B.S. and M.S. degrees in electrical engineering from National Central University, Taoyuan, Taiwan, in 2013 and 2015, respectively. Her research interests are the designs of compact microwave passive components and antennas.

WEI-TING FANG was born in Taipei, Taiwan, in 1984. He received the B.S. degree in electrical engineering from National Chiayi University, Chiayi, Taiwan, in 2011, and the Ph.D. degree in electrical engineering from National Central University, Taoyuan, Taiwan, in 2017. His research interests are the designs of compact microwave circuits and RF system-in-package modules.

YO-SHEN LIN (M'04–SM'08) was born in Taipei, Taiwan, in 1973. He received the B.S. and M.S. degrees in electrical engineering and the Ph.D. degree in communication engineering from National Taiwan University, Taipei, Taiwan, in 1996, 1998, and 2003, respectively.

From 1998 to 2001, he was a RF Engineer with Acer Communication and Multimedia Inc., Taipei, Taiwan, designing global system for mobile communication (GSM) mobile phones. From 2001 to 2003, he was with the Chi-Mei Communication System Inc., Taipei, Taiwan, where he was involved with the design of LTCC RF transceiver module for GSM mobile applications. In 2003, he joined the Graduate Institute of Communication Engineering, National Taiwan University, as a Post-Doctoral Research Fellow, and became an Assistant Professor in 2004. Since 2005, he has been with the Department of Electrical Engineering, National Central University, Taoyuan, Taiwan, where he is currently a Professor. Since 2008 he has been a Guest Researcher with the Ferdinand-Braun-Institut, Leibniz-Institut für Höchstfrequenztechnik, Berlin, Germany. From 2010 to 2013, he was the Director of Top University Program Office under the Research and Development Office, National Central University. He was a Visiting Scholar with the Department of Electrical and Computer Engineering, University of California at San Diego, San Diego, USA, from 2014 to 2015. Since 2017, he has been the Vice Chair of the Taipei Chapter of IEEE MTT-S. He has authored or co-authored over 120 international journal and conference papers, and five granted U.S. patents. His research interests include the designs of miniature microwave passive component and highly integrated RF transceiver module for wireless communication applications.

Dr. Lin was a recipient of the Best Paper Award of the 2001 Asia-Pacific Microwave Conference, Taipei, Taiwan, the URSI Young Scientist Award presented at the 2005 URSI General Assembly, New Delhi, India, the URSI EMT-S Young Scientist Award presented at the 2007 URSI International Electromagnetic Symposium, Ottawa, Canada, the 2008 Exploration Research Award of the Pan Wen-Yuan Foundation, Taiwan, the 2012 Outstanding Young Electrical Engineer Award of the Chinese Institute of Electrical Engineering, Taiwan, and the Best Symposium Paper Award of the 2015 Asia-Pacific International Symposium on Electromagnetic Compatibility, Taipei, Taiwan.